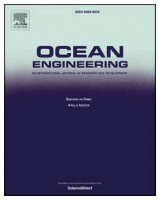
Ocean Engineering 287 (2023) 114875



Contents lists available at ScienceDirect

Ocean Engineering

journal homepage: www.elsevier.com/locate/oceaneng





Dominant factors responsible for wave modulation in the macro-tidal Gyeonggi Bay of the Yellow Sea

Ki-Hwan Kim [a], Myung-Seok Kim [a,b], Hye Min Lee [a], Myung Hwan Kim [a], Seung-Buhm Woo [a,*]

[a] Department of Ocean Sciences, Inha University, Incheon, 22212, Republic of Korea
[b] Division of Polar Ocean Science, Korea Polar Research Institute, Incheon, 21990, Republic of Korea

ARTICLE INFO

Handling Editor: Prof. A.I. Incecik

Keywords:
Macro-tidal environment
Tidal modulation
Wave dissipation
Dominant factor
Numerical modeling
Tidal flat

ABSTRACT

Surface gravity waves, crucial for sediment transport in coastal regions, undergo wave modulation owing to local hydrodynamic conditions. However, the cause of the spatial and temporal distribution of the dominant factors in wave modulation remains vague. This study was aimed at identifying the causes of tidal modulation of waves in Gyeonggi Bay, which exhibits shallow water and macro-tidal environment, and estimating site-specific dominant factors using numerical modeling. The results indicated that tides significantly impact wave dynamics at semi-diurnal tidal frequencies, with spatiotemporal variability. The most dominant factor in wave modulation in the nearshore region is the depth change caused by tides, and the most notable impact was found in tidal flats. Depth dependence is mainly evident in surf zones, with a clear distinction at locations where the wave height to water depth ratio reaches 0.2. While idealized studies highlight the significant role of wind in governing incoming waves, it is not the primary cause of modulation. Nevertheless, stronger tidal strength can lead to more pronounced modulation, which is further amplified when accompanied by strong wind conditions. This finding indicates that the spatiotemporal distribution of wave modulation in macro-tidal regions may have a significant impact on various estuarine dynamics including sediment transport.

1. Introduction

Surface gravity waves play an important role in the ocean-atmosphere interface, including the transfer of momentum, energy, heat, mass, and radiation (Cavaleri et al., 2012). In coastal regions, wind-generated waves can impact man-made structures and dominate nearshore processes on beaches and coastlines (Wolf et al., 2011). In addition, coastal sea level can be influenced by wave setup, wave run-up, and infragravity waves (Dodet et al., 2019). Therefore, waves are the primary driving force of nearshore circulation and sediment transport in the surf zone and inner continental shelf (Aboobacker et al., 2013). Understanding wave characteristics is crucial for effective coastal management.

As waves travel from the open sea toward the coast, they are subject to the influence of hydrodynamic conditions and topography (Vincent, 1979; Tolman, 1990). Time-varying water depths and ambient currents due to tides can change wave characteristics (Wolf and Prandle, 1999; Holthuijsen, 2010). Previous studies have elucidated the key mechanisms governing surface gravity waves. For example, Moon (2005) demonstrated that tides primarily drive the mean wave modulation in the Yellow and East China Seas and that the extent of the modulation depends on the tidal patterns. Ardhuin et al. (2012) revealed that currents can modulate waves and that strong currents resulting from topographical features also impede wave propagation. Bolaños et al. (2014) found that tidal fluctuations that cause changes in water depth significantly influence wave modulation in estuaries dominated by tides. In coastal regions, various factors, such as topography, tidal variations in depth and currents, and local characteristics, influence wave modulation.

Various studies have utilized field observations (Wolf and Prandle, 1999), laboratory experiments (Lai et al., 1989), and numerical modeling (Wang and Sheng, 2018) to understand the mechanisms of wave modulation. Recently, numerical modeling has been employed to evaluate the impact of various factors on waves and is considered an effective approach. Following two common conclusions can be drawn from previous studies: 1) currents dominate wave modulation in narrow channels and offshore regions; and 2) depth variation is more influential in nearshore regions (Kang and Di Iorio, 2006; Viitak et al., 2016; Li et al., 2022b). The dominant factors in wave modulation depend heavily on the local hydrodynamic conditions (Kang and Kim, 2015; Song et al., 2020). Understanding the dominant factors that affect wave modulation

* Corresponding author. Department of Ocean Sciences, Inha University, Incheon, 22212, Republic of Korea.
E-mail address: sbwoo@inha.ac.kr (S.-B. Woo).

https://doi.org/10.1016/j.oceaneng.2023.114875
Received 29 March 2023; Received in revised form 5 May 2023; Accepted 17 May 2023
Available online 11 September 2023
0029-8018/© 2023 Elsevier Ltd. All rights reserved.

is crucial, particularly in regions undergoing coastal development.

Gyeonggi Bay (GGB), located in the eastern Yellow Sea, features a complex coastline with large and small islands and shallow water. GGB holds considerable economic and ecological value owing to its abundant marine resources and strategic location. The tidal regime in this area is characterized as a macro-tidal environment, exhibiting a tidal range exceeding 8 m and a tidal current surpassing 1.5 m/s (Woo and Yoon, 2011). Based on the tidal amplitude (A) of the four tidal constituents (K_1, O_1, M_2, and S_2), the tidal form number F ($=(A_{K1}+A_{O1})/(A_{M2}+A_{S2})$) was 0.18, indicating the predominance of semidiurnal tides. Of these, M_2 is known to be the most dominant and controls the circulation patterns in this region. This region is influenced by the East Asian Monsoon, with a relatively strong north-northwesterly wind in winter and a weaker south-southeasterly wind in spring and summer (Hwang et al., 2014). In addition, high waves (>1 m) frequently propagate during winter owing to the monsoon climate. The winds and waves from the northwest in winter determine the sediment transport from the south to the west coast of Korea (Lee, 2014). In summer, high waves are often propagated by typhoons. Although they are less common than high waves in winter, waves in summer cause casualties and property damage. In addition, more than 70% of the precipitation and river discharge are concentrated in summer owing to the influence of the monsoon climate.

In GGB, where waves play an important role in sediment transport, Kang and Kim (2015) showed that wave breaking and tidal modulation of waves occur owing to depth changes induced by tides. In conjunction with these findings, Choi et al. (2014), who showed the distributions of total suspended matter (TSM) measured by the Geostationary Ocean Color Imager (GOCI), reported that the pattern of sediment transport in GGB follows the tidal cycle (Fig. 1). Hence, it is essential to understand the factors behind wave modulation and determine the dominant ones to ensure sustainable coastal management. Nevertheless, there is limited research available that focuses on identifying the spatial and temporal distributions of the dominant factors involved in wave modulation. The Korea Meteorological Administration (KMA) provides wave variables through its wave prediction system; however, this system lacks the spatiotemporal resolution required to capture wave modulation in coastal regions. Moreover, the study by Kang and Kim (2015) had a limitation in identifying the local deformation of wave characteristics owing to their use of time-varying but spatially uniform variations in depth and current across the entire model domain. This approach does not effectively reproduce the complex bathymetry and macro-tidal environment of GGB. To determine the spatial and temporal distributions of dominant factors in wave modulation, local hydrodynamic conditions need to be considered.

This study was aimed at determining the impact of depth and current on wave modulation in GGB and estimating the site-specific dominant factor. The objectives of this study were to (i) investigate the cause of wave height modulation in GGB, (ii) assess the contribution of water depth and current varying with the tidal phase (flood, ebb, high, and low tides), and (iii) estimate the site-specific dominant factor in wave height modulation over the region. The remainder of this paper is organized as follows. The analysis of the observation data is presented in Section 2. The model description and setup are described in Section 3. The model validation and results are presented in Section 4. The discussion is presented in Section 5. Finally, a summary and conclusions are presented in Section 6.

2. Wave modulation under observation

2.1. Observation data

The study area, GGB, is characterized by complex bathymetry and shallow water with an average depth of 40 m (Fig. 2). Several observation points are available for monitoring waves, tides, and atmospheric conditions in the bay. The wave variables observed in 2020 were collected using one weather buoy at Duckjeokdo (DJ) and three wave buoys at Jangbongdo (JB), Jawoldo (JW), and Ijakdo (IJ) operated by the KMA. Wave observations were conducted near the islands. Wave variables were obtained by calculating the moving acceleration of the buoy installed at sea level using the spectral method. The water depth of DJ was 30 m, and the observation was performed using a 3-m discus buoy. Non-directional wave variables (significant wave height (SWH) and peak wave period (T_{peak})) and directional wave variables (mean wave direction (θ_m)) were provided at 30-min intervals. The water depths at JB, JW, and IJ were 26, 30, and 31 m, respectively. The observation was performed using small wave buoys with a diameter of approximately 70 cm. Non-directional wave variables (SWH and T_{peak}) were provided at 1-h intervals. Atmospheric data (wind and air pressure) were provided at DJ (weather buoy). Wind data were collected using a wind speed vane meter installed at approximately 4 m above sea level. Samples were collected at a frequency of 1 Hz for 10 min. Time-averaged wind variables were provided at 30-min intervals. However, water elevation data were not provided for the four buoys. Water

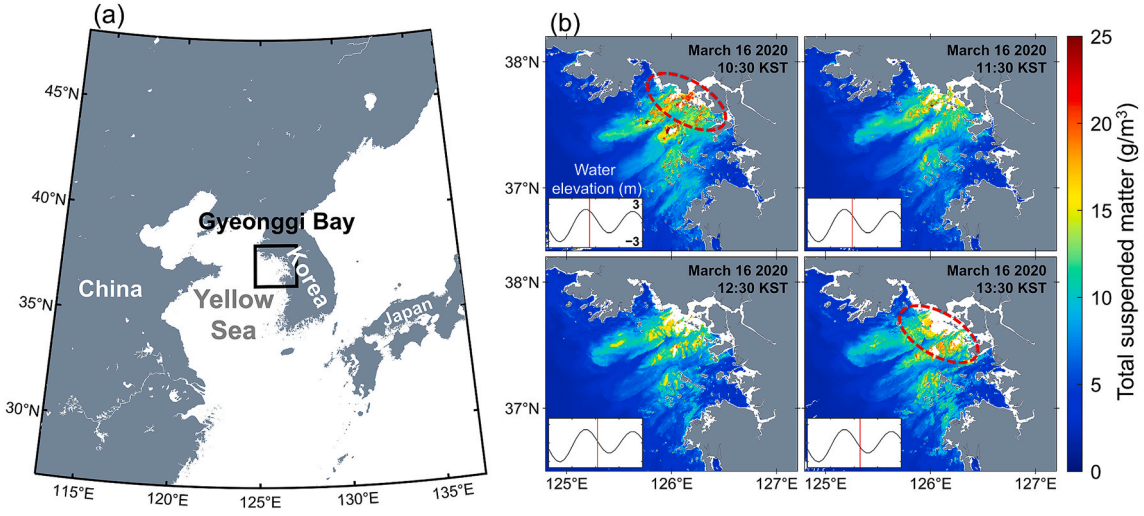


Fig. 1. (a) Location of Gyeonggi Bay (GGB) in the Yellow Sea. (b) Contour map of the total suspended matter (TSM) in GGB, derived from the Geostationary Ocean Color Imager data. The TSM data shown correspond to March 16, 2020, and each contour represents the TSM distribution at the time indicated by the red line in the time series on the left-hand side (10:30, 11:30, 12:30, and 13:30 Korea Standard Time). The red dashed circles indicate where high concentration of TSM are distributed.

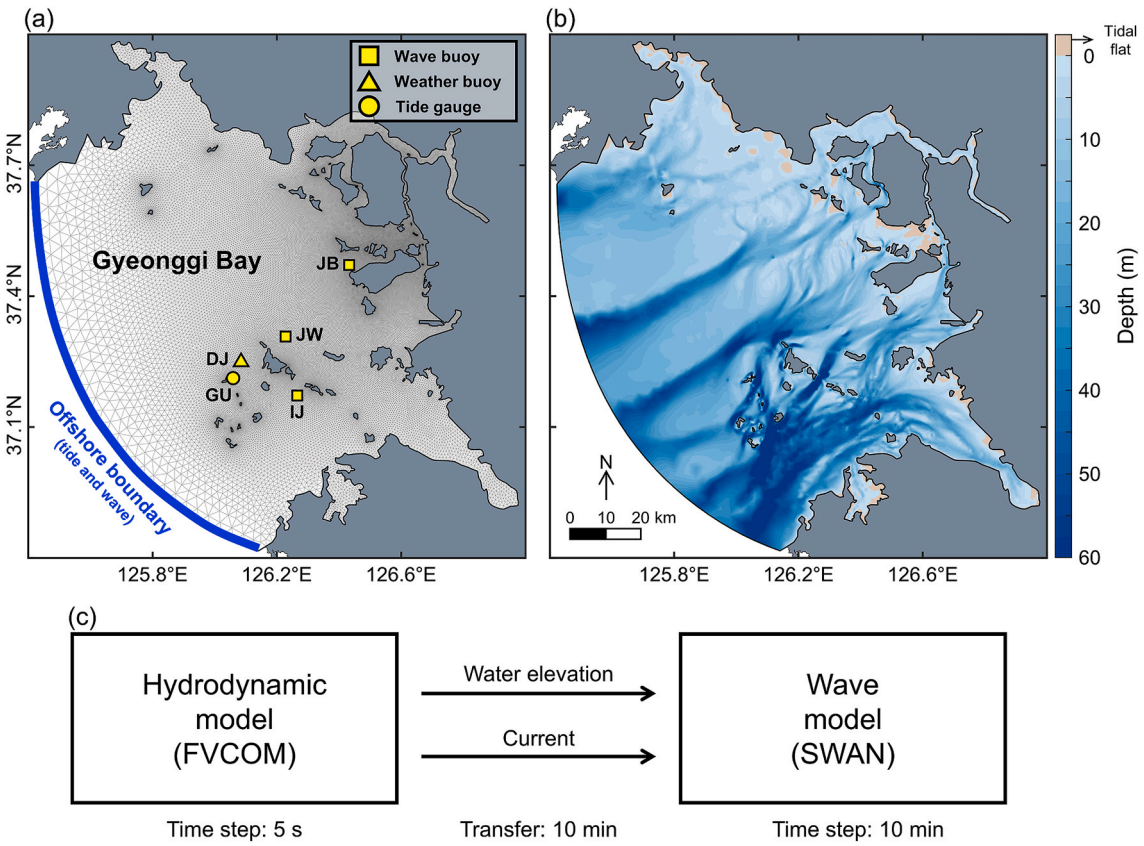


Fig. 2. (a) Model grid system and observation points. The blue line indicates the model offshore boundary where the boundary conditions of the tide and wave are entered. The observation points consist of three wave buoys, one weather buoy, and one tide gauge. (b) Model bathymetry based on the mean sea level. The gray shaded area is the area where the water depth is less than 0 m with respect to the mean sea level, and the tidal flat is distributed. (c) Graphical diagram of model simulation. The finite volume community ocean model (FVCOM) and simulating waves nearshore (SWAN) model were used.

elevation data at 1-h intervals were provided by the Korea Hydrographic and Oceanographic Agency (KHOA). The water elevation at the Gulupdo (GU) tide gauge, adjacent to the aforementioned four buoys, was used for spectral analysis and model validation.

2.2. Spectral content

The power spectra of the water elevation (at GU tide gauge) and SWH (at the four buoys) and their coherence are given in Fig. 3. For the spectral analysis, demeaned and detrended hourly data were used, a Hamming window with a length of 10 days and an increment of 2 days (80% overlap) was applied, and the degree of freedom was 358. The water elevation spectra featured peaks at diurnal and semidiurnal tidal frequencies (Fig. 3a). Among these peaks, the strongest appeared at the semidiurnal tidal frequency, showing the tidal characteristics of GGB, where the semidiurnal tide is dominant. In the SWH spectra of the four buoys, a large power appeared at low frequencies, corresponding to a period of 5–10 d (Fig. 3b). This was mainly associated with the typical timescale of wave propagation over GGB. In addition, the SWH spectra featured sharp peaks at the semidiurnal tidal frequency, especially M_2 of 1.93 cycles per day (cpd). Sharp peaks were most prominent at IJ and JB, whereas a relatively weak peak was observed at DJ.

To identify the cause of the sharp peaks in the semidiurnal tidal frequencies in the SWH spectra, a spectral coherence analysis was performed between the water elevation at GU tide gauge and SWH at the four buoys (Fig. 3c). The highest and lowest coherences at the semidiurnal tidal frequency were 0.62 at JB and 0.32 at DJ, respectively. In addition, these results showed a similar coherence pattern when calculated using the water elevations at other tide gauges (figure not shown). From the observation results, the semidiurnal SWH modulations were found to be mainly induced by the tide. Noteworthily, the influence of the tide varies according to the geographic location of the four buoys. One of the objectives of this study was to analyze the causes of SWH modulation in GGB. Therefore, DJ (the lowest coherence) and JB (the highest coherence) are discussed.

2.3. Temporal variability

The SWH modulation at semidiurnal frequencies can be examined using a wavelet transform. The time series and wavelet power spectra of the SWH at DJ and JB in 2020 are shown in Fig. 4. High waves in the winter (January–April and December) and frequent storm events in the summer (July–September) were identified. This demonstrates the seasonal variation in the SWH associated with the East Asian monsoon system of the Yellow Sea. Quantitative comparisons of the power spectra were limited owing to the different geographic locations and SWH magnitudes at DJ and JB. Therefore, the wavelet transform was performed by normalizing the observed SWH at DJ and JB by dividing them by their respective standard deviations (*SD*), as proposed by Torrence and Compo (1998). The SWH modulation was apparent at the semidiurnal tidal frequencies (period: 12 h) at JB but not DJ. The modulation at JB was proportional to the SWH, exhibiting a relatively smaller scale when SWH was low (e.g., May–July). This implies that wave modulation may be stronger during high wave periods at JB. These results also suggest that DJ may be less affected by tides than JB, supporting the coherence between water elevation and SWH (Fig. 3c).

Although the above analysis primarily focused on the role of tides in wave modulation, it is important to note that wave modulation can also be influenced by factors other than tides. For example, Wang and Sheng (2018) reported that the wave type (swell and wind sea) plays a vital

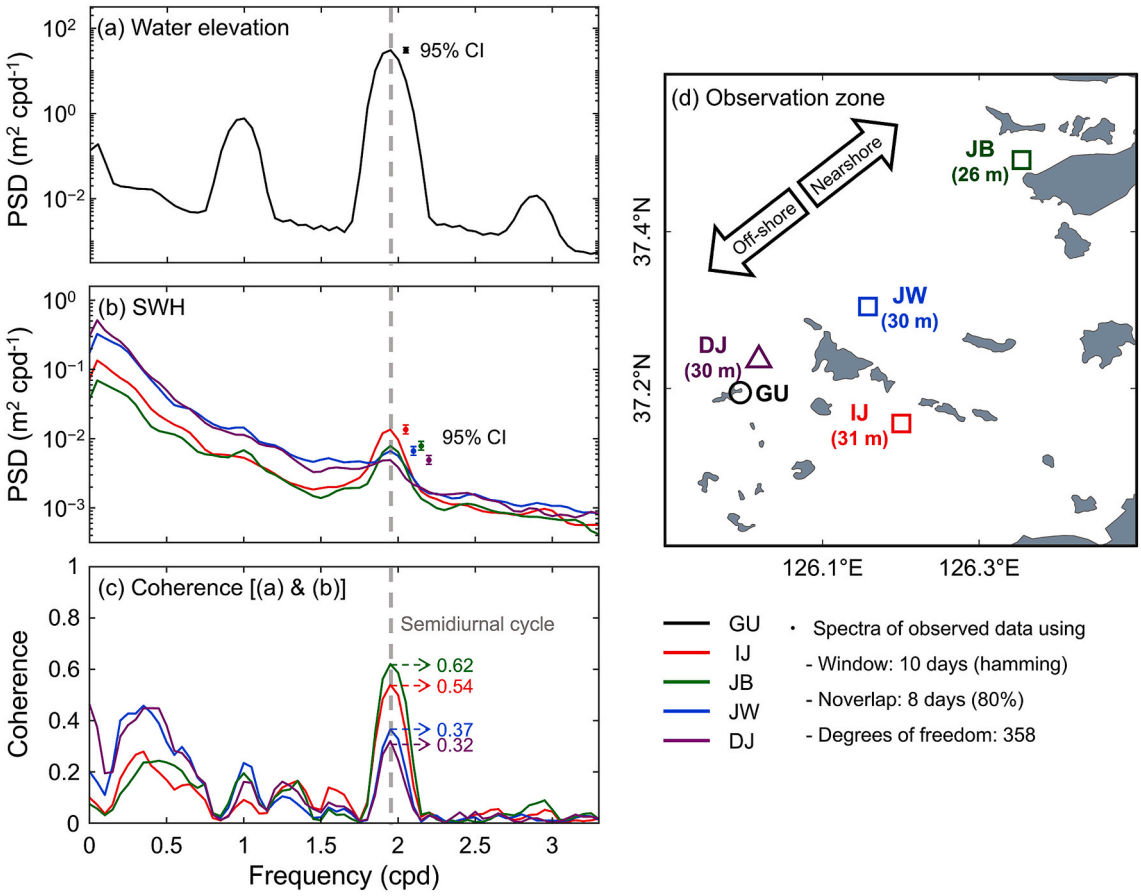


Fig. 3. Power spectral density of (a) water elevation at the Gulupdo (GU) tide gauge and (b) significant wave heights at the Jangbongdo (JB), Jawoldo (JW), and Ijakdo (IJ) wave buoys and the Duckjeokdo (DJ) weather buoy. Also shown is a cross-spectra analysis between the time series of water elevation and the significant wave heights with (c) coherence. The gray vertical dashed lines represent the semidiurnal tidal frequency. (d) The observation system includes one tide gauge (GU), three wave buoys (JB, JW, and IJ), and one weather buoy (DJ). The numbers below the buoys indicate the depth at each buoy.

role in determining the magnitude of wave modulation at tidal frequencies. Therefore, the difference in the magnitudes of SWH modulation between DJ and JB could also be attributed to the regional variation in the characteristics of the wave types. However, as the purpose of this study was not to investigate the SWH modulations according to the wave type, it was excluded from the analysis. In the following section, the cause of spatially different SWH modulations in GGB is explained using numerical modeling.

3. Methods

3.1. Modeling system

Surface wave observations can be obtained using several platforms (e.g., wave buoys, radars, and satellites). Among them, the observation data from the wave buoy are the most reliable. However, wave buoys located in the ocean are insufficient for conducting wave analyses in all regions. Because of these insufficient observations, numerical models have been used for regional surface wave studies (e.g., Moon, 2005; Yu et al., 2017). The simulating waves nearshore (SWAN) model, which is a third-generation wave model, was used in this study. Third-generation wave models that are widely used today have been developed through the reduced discrete interaction approximation parameterization of nonlinear interactions (Cavaleri et al., 2020). SWAN does not compute the water depth and current variations alone. However, time-varying depth and current are essential for the accurate modeling of wave parameters (Bolaños et al., 2014). To consider the impacts of these two factors, coupling with a hydrodynamic model or using them in the form of input data in SWAN is required. When model coupling does not proceed or is not used as input data, the variations in the water depth and current are treated as zero values, and their influence is ignored. In this study, a hydrodynamic model, namely the finite-volume community ocean model (FVCOM), was simulated for the same period as that for the SWAN model and was used as the input data. The description of each model and the model setup are described below.

3.1.1. FVCOM

FVCOM is a coastal ocean and estuarine model developed through collaboration between the University of Massachusetts-Dartmouth and Woods Hole Oceanographic Institution. It is a prognostic, three-dimensional, triangular, unstructured grid, free-surface, and primitive equation ocean model (Chen et al., 2003). The FVCOM was discretized with triangular grids in the horizontal direction and generalized terrain-following coordinates in the vertical direction. In addition, FVCOM calculates the mass flux of triangular grids using a second-order upwind finite volume method that discretizes the governing equation into an integral form. This approach well guarantees mass conservation in both the individual control elements and the entire computational domain. In addition, triangular unstructured grids are suitable for solving the problem of sea areas with complex shorelines.

3.1.2. SWAN

The SWAN model, a third-generation wave model, was developed by the Delft University of Technology in the Netherlands (Booji et al., 1999). This study utilized an unstructured grid version of SWAN (Zijlema, 2010), which performed well in regions with complex coastlines.

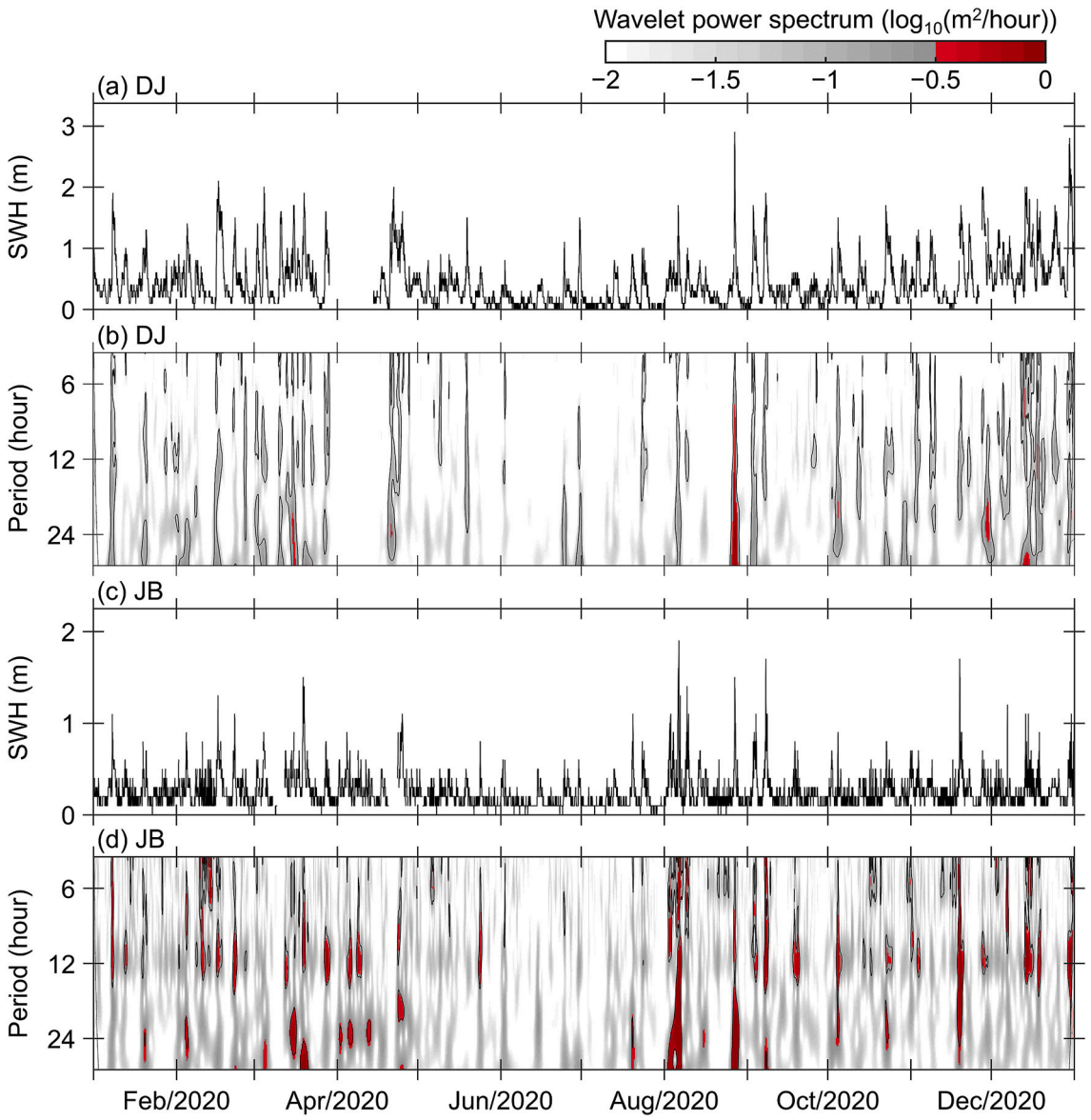


Fig. 4. Comparison of the observed wave modulations at DJ weather buoy and JB wave buoy. (a) and (c) Time series of significant wave heights (SWH) observed in 2020. (b) and (d) Wavelet power spectrum for the significant wave heights observed including a semidiurnal band (12 h, two cycles per day). The black lines enclose regions of 95% significance level for the calculated wavelet power spectra. Note that each power spectrum was normalized by its standard deviation for the comparison purpose.

SWAN simulates the evolution of a two-dimensional wave energy spectrum under varying wind, current, and water depth conditions. It considers refraction, shoaling, reflection, and diffraction due to water depth and current in the wave propagation process. SWAN employs the wave action balance equation as its governing equation to calculate the energy spectrum changes in two-dimensional horizontal space, representing the wave in the form of a wave energy spectrum, expressed as Eq. (1).

$$\frac{\partial N}{\partial t} + (\vec{c_g} + \vec{u})\nabla_{x,y} N + \frac{\partial c_\sigma N}{\partial \sigma} + \frac{\partial c_\theta N}{\partial \theta} = \frac{S_{tot}}{\sigma} \quad (1)$$

where N is the wave action density, σ is the relative frequency, and θ is the wave propagation direction. On the left-hand side of Eq. (1), the first term represents the local rate of change in the wave action density over time. The second term represents the propagation of wave energy in two-dimensional geographic space (with the group velocity $\vec{c_g}$ and the ambient current $\vec{u}$). The third term represents the relative frequency shift due to variations in the current and depth. The fourth term represents the depth- and current-induced refraction (with propagation velocity c_θ in directional space θ). The upper part of the right-hand side is a source term (S_{tot}) representing the wave generation by wind, nonlinear wave-wave interactions, and dissipations, expressed as Eq. (2).

$$S_{tot} = S_{in} + S_{nl3} + S_{nl4} + S_{ds,w} + S_{ds,b} + S_{ds,br} \quad (2)$$

where S_{in} is the wave generation by wind; S_{nl3} and S_{nl4} are the three- and four-wave interactions, respectively; and $S_{ds,w}$, $S_{ds,b}$, and $S_{ds,br}$ are the dissipation terms due to whitecapping, bottom friction, and depth-induced wave breaking, respectively.

3.1.3. Wave kinematics in SWAN

The kinematics of wave trains allows the use of linear wave theory and transforms of wave crests to obtain wave propagation speeds in spatial and spectral spaces (Whitham, 1974; Mei, 1983). The kinetic effects are considered in the second to fourth terms on the left-hand side of Eq. (1). The wave propagation velocities in the spatial and spectral

spaces are expressed by the following equations:

$$\frac{d\vec{x}}{dt} = \vec{c_g} + \vec{u} = \frac{1}{2}\left(1 + \frac{2\left|\vec{k}\right|d}{\sinh\left(2\left|\vec{k}\right|d\right)}\right)\frac{\sigma\vec{k}}{\left|\vec{k}\right|^2} + \vec{u} \tag{3}$$

$$\frac{d\sigma}{dt} = c_\sigma = \frac{\partial\sigma}{\partial d}\left(\frac{\partial d}{\partial t} + \vec{u} \bullet \nabla_{\vec{x}} d\right) - c_g\vec{k} \bullet \frac{\partial\vec{u}}{\partial s} \tag{4}$$

$$\frac{d\theta}{dt} = c_\theta = -\frac{1}{k}\left(\frac{\partial\sigma}{\partial d}\frac{\partial d}{\partial m} + \vec{k} \bullet \frac{\partial\vec{u}}{\partial m}\right) \tag{5}$$

In Eq. (3), $\vec{c_g}$ represents the group velocity, and $\vec{u}$ represents the current vector, which is assumed to be uniform in the vertical direction. The depth-averaged current was used in the study. $\vec{k}$ is the wavenumber vector, and d is the water depth. s is the spatial coordinate in the wave propagation direction of θ, and m represents the coordinate normal to s.

Eqs. (3)–(5) show that variations in depth and current affect the wave propagation velocities. When the wave and current travel in the same (opposite) direction through the kinematics in the spatial and spectral spaces, the values of the second and third terms in Eq. (1) become larger (smaller). Accordingly, the wave energy becomes larger (smaller), and the wave height also increases (decreases). Moreover, when the depth of the coastal region decreases, the group velocity of the wave also decreases, causing an increase in the energy density to maintain a constant wave energy flux. This result can cause an increase in the wave height.

3.2. Model setup

The magnitude of the SWH modulation in GGB was consistent with that of the SWH (Fig. 4d). Selecting a model simulation period that includes high waves to simulate SWH modulation is necessary. The period of high waves was defined as a section exceeding the SWH by 1 m, which was twice the average SWH observed at the outermost buoy (DJ) in GGB. The period under analysis was February 14–20, 2020, a time frame with high waves persisting for more than two days and minimal missing observational data. To ensure stability, the model simulations ran up to this analysis period, including a 5-day spin-up time. Moreover, during this period, sediment transport was known to be dominated by wave action in the eastern Yellow Sea (Lee, 2014).

For simulating the wave dynamics, FVCOM and SWAN models were employed on the same grid, which consisted of 51,336 nodes and 98,441 cells. The unstructured grid had a horizontal resolution ranging from a maximum of 4,500 m at the offshore boundary to a minimum of 90 m in the nearshore region (Fig. 2a). The model bathymetry was constructed by combining KorBathy30s (Seo, 2008) and BADA Ver. 1 (Yoo et al., 2019) datasets, which are based on the approximate lowest low water. However, FVCOM and SWAN were calculated based on the mean sea level. To account for the discrepancy between the approximate lowest low water and mean sea level, the difference provided by KHOA for 2020 was incorporated into the bathymetry datasets.

The atmospheric data used in the model calculations were obtained from the Local Data Assimilation and Prediction System (LDAPS), operated by the KMA. LDAPS performs eight model runs every day with 3-h intervals and provides atmospheric data at 1-h intervals. LDAPS covers the Korean Peninsula and has a grid resolution of 1.5 km. The model consists of 70 layers up to approximately 40 km vertically and uses the Arakawa C-grid and Charney-Philips staggered grid systems. For this study, the mean sea level pressure (MSLP) and a 10-m wind field (U10, V10) were used. For more information on the LDAPS, refer to Kim et al. (2022).

In the FVCOM simulation, both tidal and atmospheric forcings (MSLP and 10-m wind field) were considered. The tidal forcings at the model offshore boundary were based on the TPXO9-atlas global tidal model (Egbert and Erofeeva, 2002), which includes eight tidal harmonic constants (M_2, S_2, N_2, K_2, K_1, O_1, Q_1, and P_1). Corrections are necessary to apply the global model results to coastal regions. The eight tidal harmonic constants are the major components of the Yellow Sea, and at least 183 days of numerical simulations were required to separate each constant (Byun et al., 2023). Therefore, each constant for the boundary conditions was adjusted using the outcomes of a seven-month simulation. Atmospheric forcings at the model surface boundary provided by LDAPS were used, and wind-driven current and water level fluctuations due to barometric pressure were considered. As the simulation period was in winter, the effect of freshwater discharge from rivers was deemed insignificant and was not considered.

In SWAN, the variation in water level and depth-averaged current from FVCOM and the 10-m wind field from LDAPS were considered. Waves propagating in the outer region of GGB were also considered under the model offshore boundary conditions. The wave variables used in the offshore boundary were taken from the Coastal WAVEWATCH III (CWW3) wave model operated by the KMA. The horizontal resolution of CWW3 was 1 km. CWW3 performs a 24-h prediction twice daily (00 and 12 KST, UTC+09 h) and provides wave variables (SWH, θ_m, and T_{peak}) at 3-h intervals. The wave variables were interpolated and used under the model offshore boundary conditions.

SWAN was simulated to reproduce both normal and high waves with a directional bin width of 10° and the Komen whitecapping effect (Komen et al., 1984). The whitecapping parameters are required to be calibrated to increase the accuracy of the wave height and wave period simulations (Allahdadi et al., 2019). This study used the power of steepness normalized with the wave steepness of a Pierson-Moskowitz spectrum of 3 to calibrate the overestimated SWH (Sun et al., 2022). Default settings were used for the other physical parameters that were not mentioned. The integration time steps for the FVCOM and SWAN simulations were 5 and 600 s, respectively. The variations in water depth and current from FVCOM were transferred to SWAN at 600-s intervals. Because they were used as input data, the wave effects on the water levels and currents were not considered. The SWAN output was requested once every 600 s.

Table 1
Description of wave model (SWAN) simulation.

Model case	Wave model (SWAN)	Hydrodynamic model (FVCOM)
Run-w	Wind and offshore wave	
Run-w+cu		Current
Run-w+dep		Depth (water elevation)
Run-w+cu+dep		Current and depth (water elevation)

Table 2
Model validation.

Variable	Station	r	IOA	RMSE
Water elevation (m)	GU	0.99	0.99	0.26
Wind speed (m/s)	DJ	0.94	0.97	1.46
Significant wave height (m)	IJ	0.80	0.69	0.31
	JB	0.86	0.84	0.17
	JW	0.87	0.75	0.26
	DJ	0.83	0.80	0.28

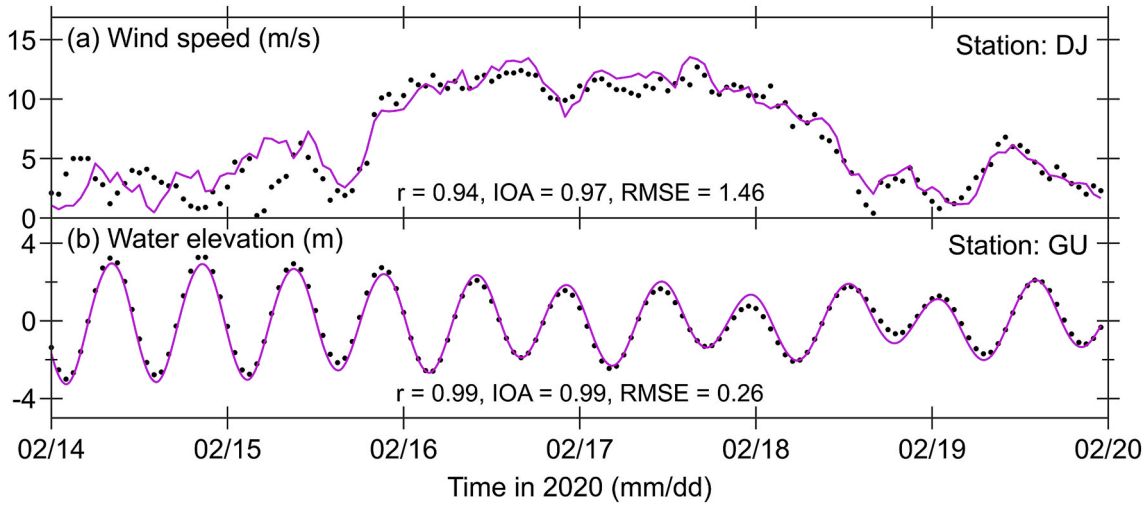


Fig. 5. (a) Wind speed at the DJ weather buoy during the simulation period (February 14–20, 2020). The black dot and purple line represent the observation data and model input data (LDAPS, atmospheric model system operated by the Korea Meteorological Administration), respectively. (b) Observation data time series of the water elevation at the GU tide gauge. The black dot and purple line represent the observation data and model input data (hydrodynamic model: FVCOM), respectively. To evaluate the input data, the correlation coefficient (*r*), index of agreement (IOA), and root mean squared error (RMSE) were calculated during the model simulation period.

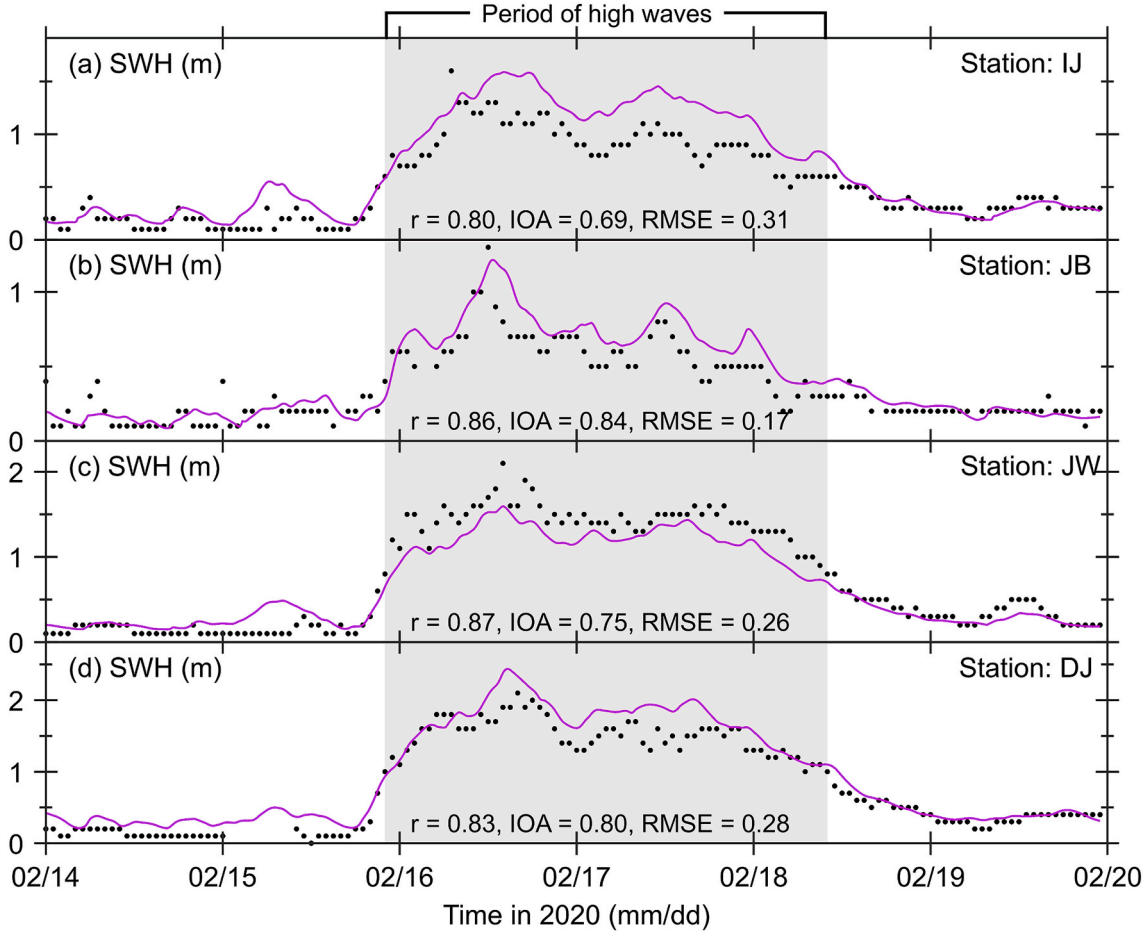


Fig. 6. Time series of the observed (black dot) and modeled (purple line) significant wave heights at IJ, JB, and JW wave buoy and DJ weather buoy during the model simulation period (February 14–19, 2020). The gray shaded area highlights the period of high waves at the DJ (SWH_{DJ} >1 m). To evaluate the modeled significant wave heights, the correlation coefficient (*r*), index of agreement (IOA), and root mean squared error (RMSE) were calculated during the period of high waves.

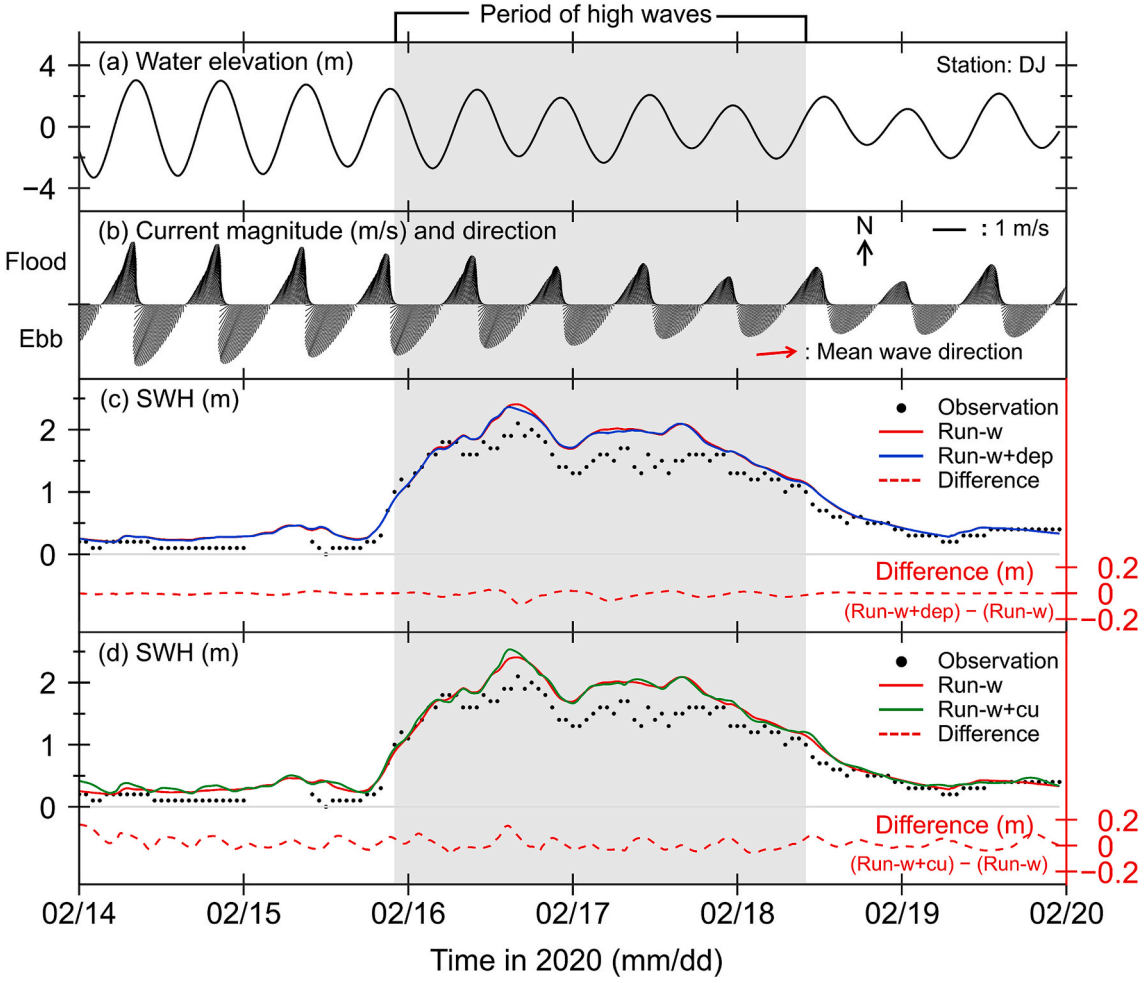


Fig. 7. Modeled (a) water elevation and (b) tidal current at the DJ weather buoy during the model simulation period (February 14–19, 2020). The gray shaded area indicates the period of high waves (see Fig. 6). Time series of (c) and (d) shows the significant wave height and the difference (red dashed line) in significant wave height due to depth and current. The black dot represents the observation data, and the red, blue, and green lines represent the Run-w, Run-w+dep, and Run-w+cu modeled data, respectively. The difference refers to the significant wave height that has been deformed by depth and current.

3.3. Model runs and statistics

Four scenarios were controlled by adjusting the water depth and current transferred from FVCOM to SWAN (Fig. 2c), as summarized in Table 1. In Run-w, waves developed by the wind and propagating offshore were considered. Run-w+cu and Run-w+dep were simulated to investigate the effects of the current and depth (caused by water level changes), respectively, on the wave field. Run-w+cu+dep was simulated to evaluate the combined impact of current and depth and was validated against the observation data. The performance of the model was evaluated using three statistical indicators: the Pearson correlation coefficient (r), index of agreement (IOA), and root mean squared error (RMSE) (Eqs. (6)–(8), respectively).

$$r = \frac{\sum_{i=1}^{n}(O_i - \overline{O})(M_i - \overline{M})}{\sqrt{\sum_{i=1}^{n}(O_i - \overline{O})^2}\sqrt{\sum_{i=1}^{n}(M_i - \overline{M})^2}} \tag{6}$$

$$IOA = 1 - \left[\frac{\sum_{i=1}^{n}(M_i - O_i)^2}{\sum_{i=1}^{n}(|M_i - \overline{O}| + |O_i - \overline{O}|)^2}\right] \tag{7}$$

$$RMSE = \sqrt{\frac{1}{n}\sum_{i=1}^{n}(M_i - O_i)^2} \tag{8}$$

where O is the observation data, M is the model data, and n is the number of elements. $\overline{O}$ and $\overline{M}$ represent time-averaged observation and model data, respectively. The model validation results are presented in Table 2.

To assess the effects of depth and current variation on SWH modulation, the normalized local RMSE difference (NRD) proposed by Moon (2005) was utilized. The NRD value quantifies the change in SWH by depth and current, using Run-w as the baseline. For example, when the NRD value is calculated using Run-w and Run-w+cu+dep, it is expressed by Eq. (9).

$$NRD = \frac{\sqrt{\frac{1}{n}\sum_{i=1}^{n}\left(SWH^{Run-w+cu+dep} - SWH^{Run-w}\right)^2}}{\frac{1}{n}\sum_{i=1}^{n}SWH^{Run-w}} \tag{9}$$

where SWH^{Run} is the model case and n is the number of data used for comparison.

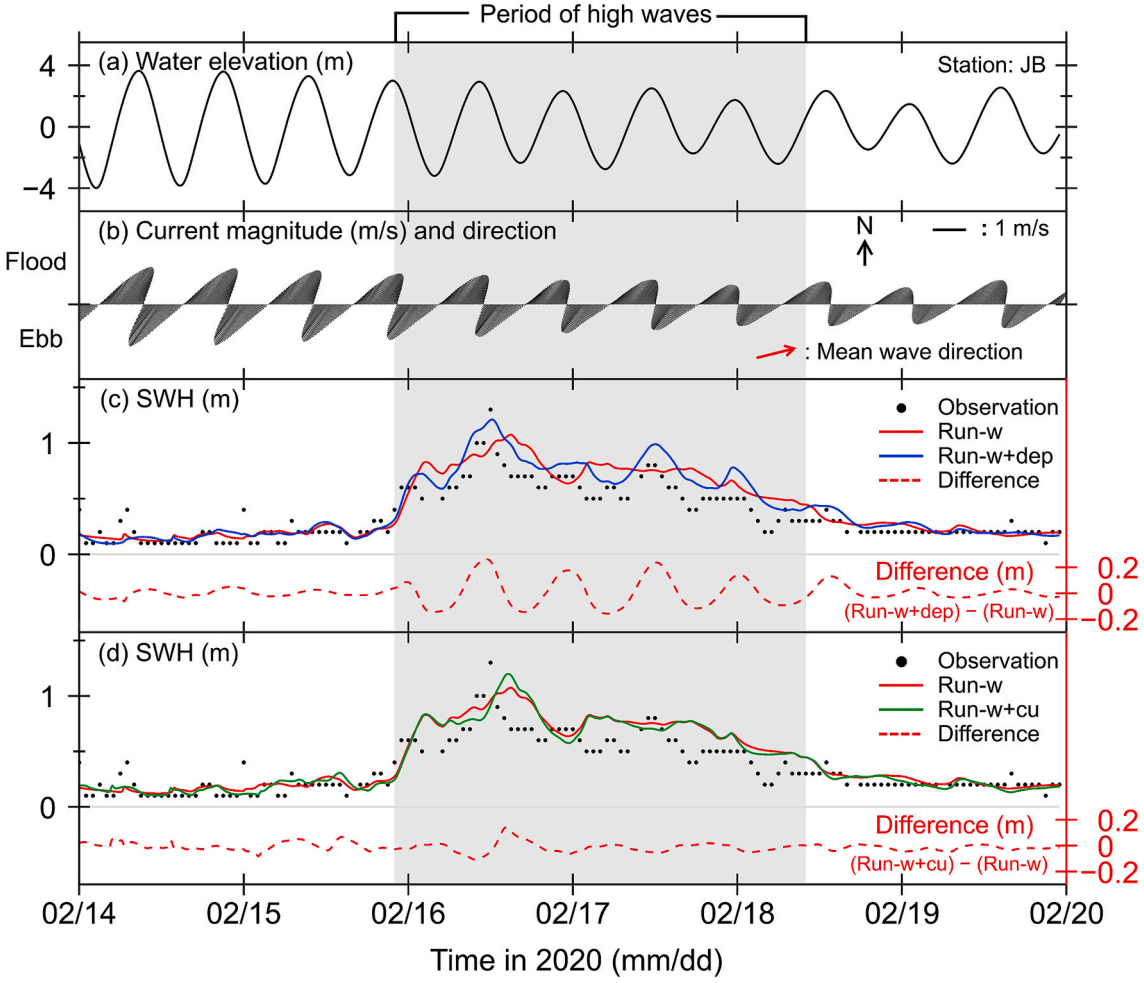


Fig. 8. As in Fig. 7, but for the JB wave buoy.

4. Model results

4.1. Model validation

The model performance was evaluated by comparing the modeled and observed data. The 10-m wind speed from LDAPS demonstrated good agreement with that observed at DJ (Fig. 5a). During the model simulation, the maximum wind speed was approximately 12 m/s, and wind speeds of 5 m/s or less were observed, except during periods of high waves. The wind direction was predominantly northwesterly (figure not shown), which is typical during the winter season in GGB (Lee, 2014). The simulated water level in FVCOM used for SWAN input also matched well with the observed water elevation at GU (Fig. 5b). As can be seen in the figure, the spring-neap tidal signal and diurnal inequality were confirmed, and a tidal range of approximately 5 m occurred during the period of high waves. Fig. 6 indicated that the modeled SWH under the impacts of current and depth (Run-w+cu+dep) at the four buoys exhibited good performance. The SWH was validated during periods of high waves, because the magnitude of the SWH modulation appeared to be large during the period of high waves (Fig. 4d). In addition, the model accuracy is relatively higher if the validation is performed over the entire simulation period. The statistical indicators of the SWH calculated during the period of high waves were in the following ranges: r, 0.80–0.87; IOA, 0.69–0.84; and RMSE, 0.17–0.31.

4.2. Impact of depth and current on SWH modulations

The impacts of depth and current on waves are very complex and significantly affected by their strength and spatial distribution (Tolman, 1990). The magnitude of the SWH modulation confirmed in Fig. 4 is determined as the sum of the magnitudes of the depth- and current-induced SWH modulation. At DJ, the water elevation ranges from approximately −3 to 3 m, and the depth-averaged current vector demonstrates dominance in the north-south direction, with an asymmetric current pattern (Fig. 7a and b). The magnitudes of the depth- and current-induced SWH modulations are shown in Fig. 7c and d, respectively. The black dots denote the observation data, and the red, blue, and green lines on the left axis represent the time series of Run-w, Run-w+dep (considering the impact of depth), and Run-w+cu (considering the impact of the current), respectively. The red dashed line on the right axis denotes the magnitude of the depth-induced (Run-w+dep − Run-w) and current-induced (Run-w+cu − Run-w) SWH differences. The model results indicate good results by Run-w at DJ. This implies that SWH modulation due to depth and current was not significant at DJ. The differences due to depth were calculated in the range from −0.09 to 0.03 m, and the maximum difference was calculated at low tide during the period of high waves. The differences due to current were calculated in the range from −0.07 to 0.16 m. Current-induced differences appeared during the ebb tide (positive) and flood tide (negative). The NRD values due to depth and current obtained during the period of high waves were 0.014 and 0.024, respectively. This implies that the impact of current on SWH modulation was approximately 70% stronger than that of depth at DJ.

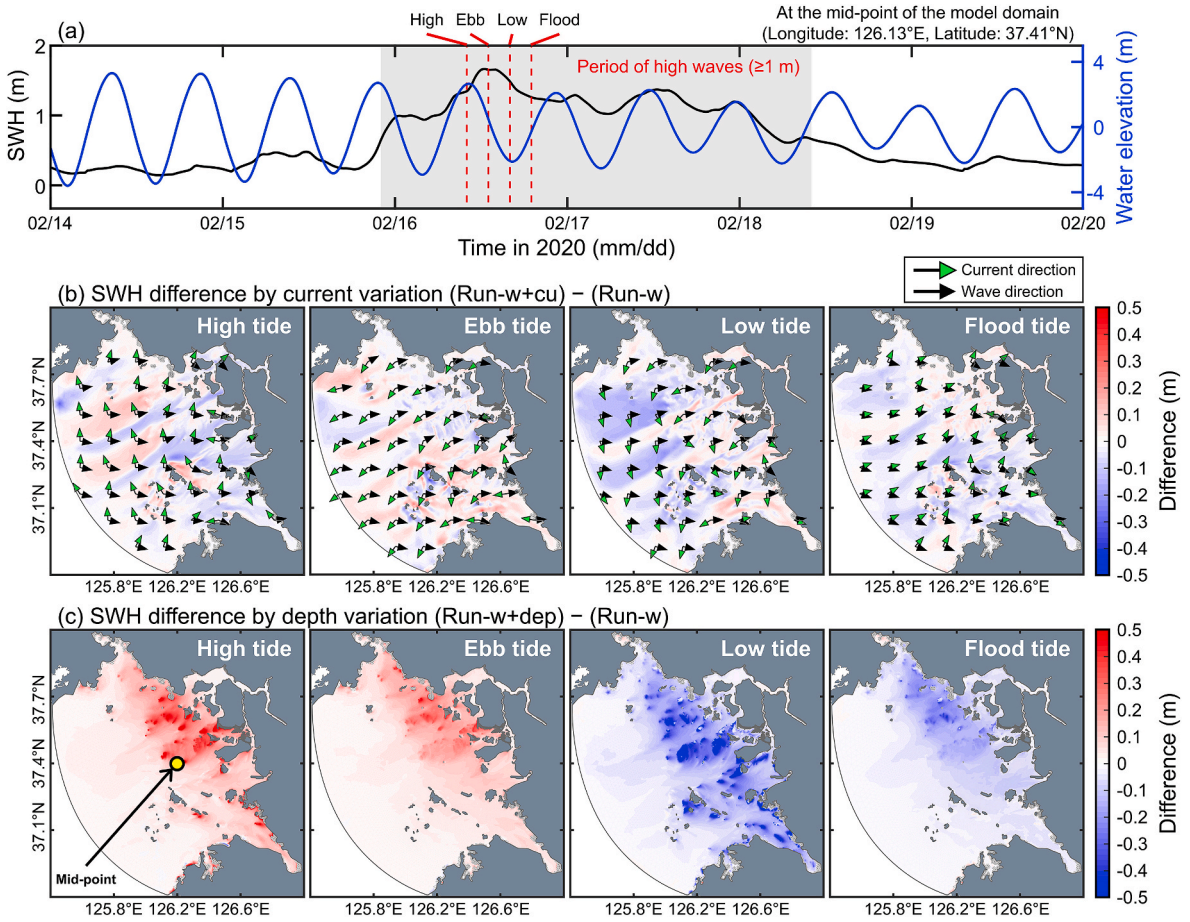


Fig. 9. (a) Modeled significant wave height and water elevation time series at the mid-point of the model domain (longitude: 126.13°E and latitude: 37.41°N) during the period of model simulation. The gray shaded area highlights the period of high waves, and the red dashed lines indicate each tidal phase (high, ebb, low, and flood tide). (b) and (c) represent the difference in significant wave height due to changes in depth and current according to each tidal phase. The magnitude of differences is expressed in color. The red (blue) color indicates that the significant wave height is increased (decreased) by depth and current. The green vector indicates the current direction, and the black vector indicates the wave direction in (b). The yellow circle indicates the mid-point of the model domain represented in (a).

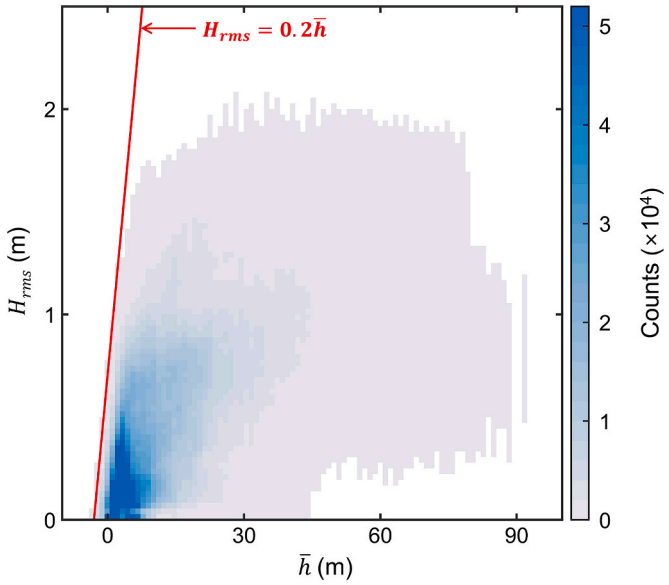


Fig. 10. A two-dimensional histogram according to mean water depth ($\bar{h}$) and root mean square wave height ($H_{rms} = \sqrt{8m_0}$, where m_0 is a high-pass filtered variance of the water surface elevation) during the period of high waves (see Fig. 6). The red line indicates an envelope line representing the ratio of H_{rms} to $\bar{h}$. The slope of the line was calculated as 0.2, and most of the histograms are located below the line.

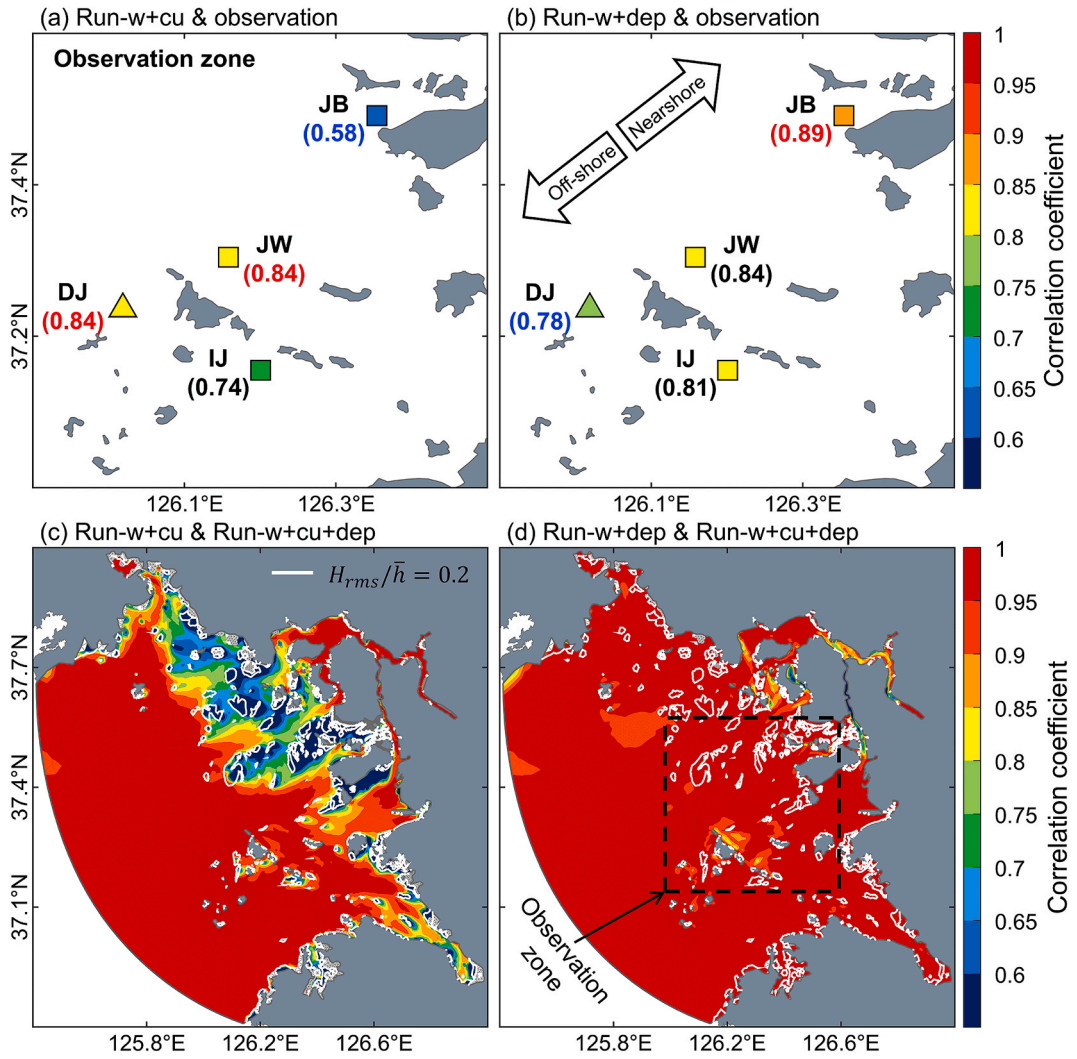


Fig. 11. Cross-correlation coefficients (a and b) between the modeled and observed significant wave heights, and (c and d) between the modeled wave heights. The number under each observation point indicates the correlation coefficient at each observation point, and the text in red (blue) indicates the highest (lowest) correlation coefficient. The white line indicates the $H_{rms}/\bar{h} = 0.2$ (see Fig. 10), and the black dashed box indicates the observation zone, which is represented in (a and b).

Fig. 8 shows the results of JB using the same layout as that in Fig. 7. The water elevation appeared in the range of approximately −4 to 4 m, and the depth-averaged current vector showed a dominant flow pattern in the northeast and southwest directions (Fig. 8a and b). The results for JB revealed enhanced model accuracy when depth variations were taken into account, especially for the SWH phase. The depth-induced SWH differences during the period of high waves ranged from −0.16 to 0.26 m, with the phase-locked pattern depending on the water elevation (Fig. 8c). In other words, increases and decreases in SWH follow the rise and fall in the water level. These patterns were found in prior studies (Kang and Kim, 2015; Yu et al., 2017) and are caused by dissipation owing to bottom friction changes and depth-induced wave breaking. The current-induced SWH differences ranged from −0.11 to 0.14 m and appeared during the ebb (positive) and flood (negative) tides (Fig. 8d). The NRD values due to depth and current, during the period of high waves, were 0.17 and 0.06, respectively. The modulation due to depth was approximately 2.8 times greater than that of the current. This suggests that depth is a dominant factor in SWH modulation at JB.

The comparison between the results of DJ (Fig. 7) and JB (Fig. 8) showed that the pattern of current-induced SWH differences increased (decreased) during ebb (flood) tides for both DJ and JB. However, the most notable difference was observed in depth-induced SWH modulation, which was likely due to the ratio of water depth to tidal strength (Moon, 2005). During the period of high waves, the depth-to-water-elevation ratios at DJ and JB were calculated to be 0.2 and 0.31, respectively. This suggests that the impact of depth was more significant at JB, where the changes in water elevation relative to water depth were larger. This finding aligns with the cross-spectral analysis (Fig. 3c) of the observed water elevation and SWH, which indicated that wave modulation by water elevation was more apparent at JB (high coherence) than at DJ (low coherence).

4.3. Contribution of water depth and current varying with tidal phase

GGB being a macro-tidal region, significant changes were expected to occur according to the tidal phase. The depth- and current-induced SWH differences at each tidal phase, including flood, high, ebb, and low tides, were analyzed (Fig. 9). The water elevation at the mid-point of the model domain (first panel of Fig. 9c) was used to define each tidal phase, with the red vertical dashed lines denoting each phase (Fig. 9a). The current-induced SWH difference (Run-w+cu − Run-w) revealed an increase and decrease in the SWH according to the relative direction of the wave and current, which was consistent with the general theory of wave-current interaction (Fig. 9b). The maximum and minimum SWH

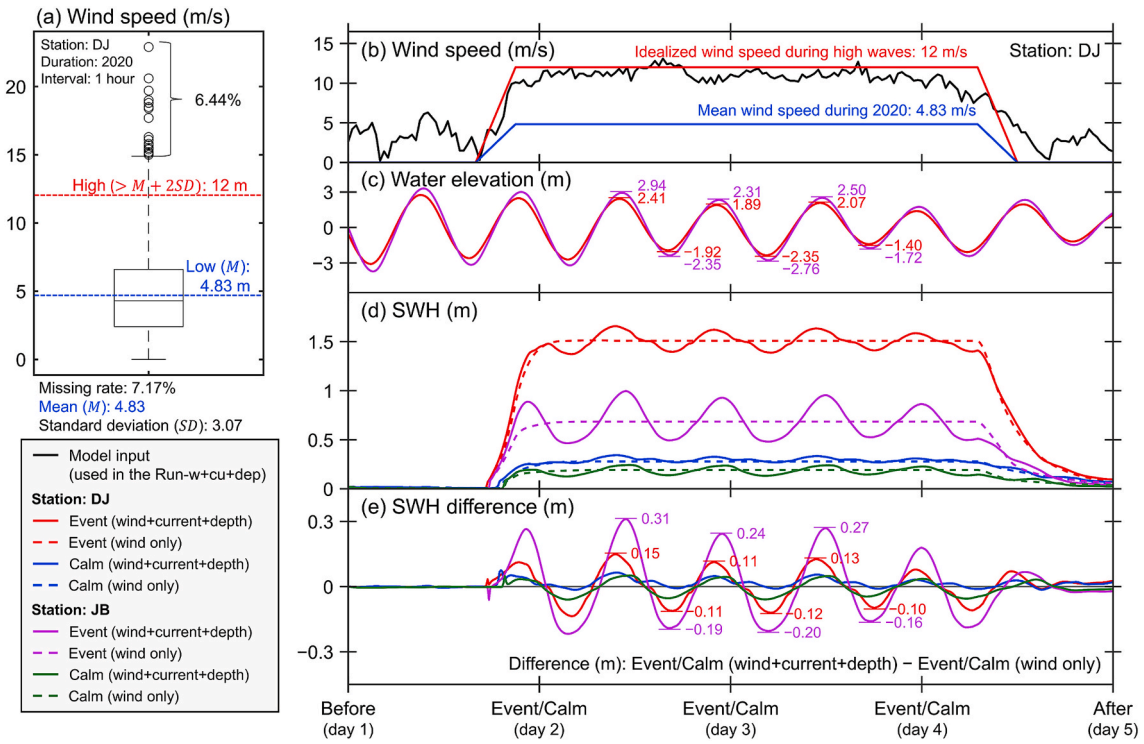


Fig. 12. (a) Box plots of wind speed observed at hourly intervals at DJ weather buoy in 2020. The percentage signs above the range of the box plots indicate the proportion of extreme wind speeds. (b) Wind speeds used in the Run-w+cu+dep simulation at DJ, along with the wind speeds used during the event ($> M + 2SD$) and calm periods (M). (c) Water elevation time series at DJ and JB wave buoy to show tidal phase and strength. (d) Time series of simulated SWH at DJ and JB, with the wind-only case represented by dashed lines. (e) SWH differences represent the variations due to tides (current and depth). The numbers in (c) and (e) indicate the maximum values of the water level and SWH differences at each tidal phase.

differences were calculated as 0.51 m (ebb tide) and −0.38 m (flood tide), respectively. However, the patterns varied across the entire model domain because the current direction and magnitude were inconsistent in all model domains owing to complex marine environments (e.g., topography). In contrast, depth-induced SWH differences (Run-w+dep − Run-w) were more pronounced (Fig. 9c). These differences were particularly noticeable at high tide (the first panel) and low tide (the third panel), with calculated ranges of −0.39 to 1.01 m and −0.93 to 0.30 m, respectively. Furthermore, these differences were particularly significant near tidal flats, where depth changes caused by tides are increasingly substantial. Two primary factors contributed to these differences. First, more wave energy propagates to the nearshore region at high tide owing to the increased water level compared with that at low tide (Tolman, 1990; Kim et al., 2008). Second, waves feel the bottom and dissipate more energy owing to the increased bottom friction at low tide when the water level is lower (Kang and Di Iorio, 2006).

5. Discussion

5.1. Possible reasons for the dominance of wave modulation by water depth

The difference in SWH with respect to depth changes due to tides was pronounced in GGB (Fig. 9). This depth dependence of wave heights mainly appears in surf zones, where local water depths control the heights of the breaking waves (Thornton and Guza, 1982; Kim, 2003). Therefore, to better understand the depth dominance of wave modulation in GGB, investigating the relationship between depth and SWH was necessary. A commonly used method to estimate this relationship is through the wave height to water depth ratio, which is calculated using the root mean square wave height ($H_{rms} = \sqrt{8m_0}$, where m_0 is the high-pass filtered variance of the water surface elevation) and mean water depth ($\overline{h}$) (Thornton and Guza, 1982; Power et al., 2010). The relationship between these two variables during the periods of high waves is illustrated using a two-dimensional histogram scatterplot (Fig. 10). Most histograms show high densities within a depth of approximately 15 m, which is due to the high resolution of the model in nearshore regions (range of resolution: 90–4,500 m). The histograms are restricted to within the red line ($H_{rms}/\overline{h} = 0.2$). In other words, the H_{rms} did not exceed 0.2 times $\overline{h}$, even during high waves. The nearshore regions are more affected by depth variations owing to the following reasons: 1) the study region is macro-tidal, and changes in water depth due to tides are larger than those in the outer region; and 2) due to shallow water environments, wave shoaling and wave breaking have stronger effects than other interactions.

The dominance of wave modulation by water depth has also been found in other coastal regions with macro-tidal environments. Sirisha et al. (2023) demonstrated a strong correlation between changes in water depth, increased wave modulation, and higher dissipation of wave energy. These effects were more pronounced closer to the shoreline. From this perspective, waves on tidal flats are expected to be more strongly influenced by changes in water depth. Unlike the inner-shelf environment, tidal flats exhibit complexity owing to the periodic changes in water depth. Because of this characteristic, the development of waves in the tidal flat is limited by the water depth, which is similar to the process in the surf zone (Le Hir et al., 2000; Li et al., 2022a). For example, Kim (2003) showed a discrepancy between two storm wave intensities in a tidal flat along the west coast of Korea and suggested that the change in water depth due to tides is the main factor determining the magnitude of the wave height. Tidal flats in GGB cover 42% of the total tidal flats (2,085 km^2) along the west coast of Korea (An et al., 2022). Therefore, the influence of depth changes on waves may be more pronounced than in other regions where tidal flats are not as widely distributed.

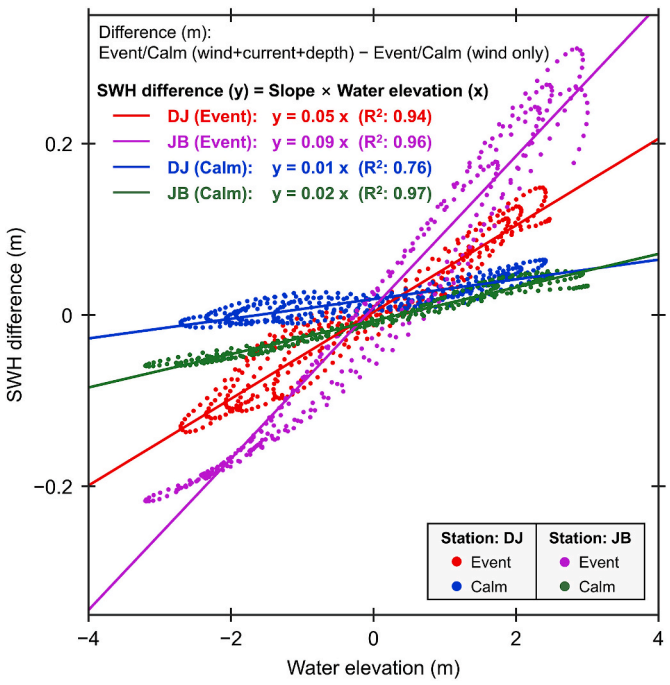


Fig. 13. Scatter plot comparison between SWH difference and water elevation at DJ weather and JB wave buoys. For the SWH difference and water elevation, refer to Fig. 12. The colored lines indicate linear regression lines.

5.2. Dominant factor in periodic wave modulation

To estimate the dominant factor in wave modulation, researchers have widely used two methods through numerical simulations (Song et al., 2020). The first method evaluates the impact of depth and current on wave modulations at a specific location based on the differences between the simulated waves. The second method calculates the spatial correlations between the wave parameters, depth, and current. The dominant factors were estimated with spatial correlation analysis, given that the individual impact of depth and current had already been confirmed at DJ (outer region) and JB (nearshore region) buoys, as shown in Figs. 7 and 8. During the period of high waves, the correlation coefficients were calculated based on the observed SWH and Run-w+cu+dep (combined action) with Run-w+dep (impact of depth on waves) and Run-w+cu (impact of current on waves).

The correlation coefficients calculated with the observed SWH at the four buoys showed distinct differences depending on the geographic locations (Fig. 11a and b). At DJ, where the current effect was stronger than depth (Fig. 7c and d), the highest correlation for Run-w+cu was obtained (0.84). However, at JB, where depth appeared to be the dominant factor in wave modulation (Fig. 8c and d), the highest correlation for Run-w+dep was obtained (0.89). For IJ, the correlations were 0.74 (due to the current) and 0.81 (due to the depth), indicating that depth changes have a more considerable influence, which is supported by the observed SWH and water elevation coherence results (Fig. 3c). Notably, identical values (0.84) were obtained at JW in both cases, suggesting the relatively lesser impact of hydrodynamic conditions on the wave modulation at JW during the model simulation.

The contrasting results between depth and current were also confirmed by the calculation results for Run-w+cu+dep (Fig. 11c and d). The white lines in both figures represent the locations where the H_{rms} is no more than 0.2 times $\bar{h}$ (see Fig. 10). In the simulation that considered only the current effect (Run-w+cu), the correlation in the nearshore region decreased to below 0.6 and showed low values (Fig. 11c). This suggests that wave modulation in these regions is predominantly controlled by depth (as indicated by the high correlation of 0.95 or higher when considering the depth effect). Noteworthily, the location where the low correlation was calculated and the $H_{rms}/\bar{h} = 0.2$ lines tended to coincide with each other. These results can be interpreted together with those of a previous study (Kang and Kim, 2015), suggesting a strong correlation between wave height and depth-induced wave breaking in GGB. This suggests that, based on where wave breaking by depth occurs, the impact of current on wave modulation is reduced, and wave modulation by depth can be dominant.

When considering only the depth effect (Run-w+dep), low correlations were found in the narrow channels (Fig. 11d). This highlights that narrow channels and straits are characterized by strong currents during flood and ebb tides, which may impact wave propagation and modulation (Ardhuin et al., 2012). However, some areas in the outer region of GGB, including the location of JW, showed high correlation coefficients in both cases. This indicated a relatively low impact of depth and current on waves in these areas and wind-induced wave generation to be the most important factor.

As reported in previous studies (Bolaños et al., 2014; Yu et al., 2017), wave modulation by depth is dominant in nearshore regions, whereas wave modulation by currents is more prominent in narrow channels. This indicates that the dominant factor in wave modulation can vary depending on the local hydrodynamic conditions. Considering the influence of waves on the surrounding environment, understanding site-specific factors in wave modulation is crucial, particularly in the case of GGB, where waves play an important role in sediment transport in the coastal region. The results of this study can be interpreted in conjunction with sediment transport patterns such as sediment suspensions. Choi et al. (2014) showed that, during winter (when the influence of waves is strong), the TSM concentration was relatively high and followed tidal cycles (see Fig. 1). Future studies that investigate the contribution of tidal modulation of waves to sediment transport, along with the impact of wave modulation, could yield more comprehensive and insightful results.

5.3. Assessment of wave modulation in tidal motion

In this study, the impacts of tidal changes in depth and current on wave heights during periods of high waves in GGB were analyzed. However, quantitatively demonstrating the impact of tides on wave modulation is difficult. To validate the impact of tides, four cases were simulated by adjusting the tidal input during the event and calm periods (Fig. 12). Model simulations were conducted over the same period, including the high wave periods used in the previous analysis, and the same tide input was applied to consider the effect of local deformation due to tides. Wind speeds during the event and calm periods were time-varying but spatially uniform across the model domain and were input in the form of a box function. For the maximum wind speed, the time-averaged wind speed observed at DJ in 2020 (mean (M), 4.83 m/s) and the idealized wind field during the periods of high waves ($>M + 2SD$, 12 m/s) were used (Fig. 12b). The wave variables used in the offshore boundary were not used as they can overestimate waves under low wind conditions. The SWH of each case was analyzed at DJ and JB locations, and the difference between the wind-only case and that including the effects of current and depth was calculated to determine the impact of tides on waves (Fig. 12e). In summary, four cases were selected to examine the formation of waves by wind speed during the event and calm periods and the modulation of waves by tides.

When considering only the impacts of wind, the SWH was found to increase and decrease with wind speed. This also shows that the wind is not a major source of periodic wave modulation when the wind direction is almost constant, as is the case during periods of high waves. When the impact of tides (depth and current variations) was added, wave modulation was observed in both the event and calm periods. In particular, the modulation during the event period was larger, with the largest modulation of 0.31 m at JB (Fig. 12e). In contrast, in the calm period,

both DJ and JB showed relatively small SWH differences within 0.05 m. Additionally, through idealized simulation, the magnitude of SWH modulation was found to depend on both wind speed and tidal strength (Fig. 13): 1) stronger winds led to increased wave modulation; 2) the stronger tidal tides strength (larger water elevation) increased the magnitude of SWH modulation. This suggests that when strong winds coincide with a spring tide, which is characterized by a substantial tidal range, wave modulation may be more pronounced.

As waves approach coastal regions, they are subjected to various external forces that can significantly affect their dynamics (Vincent, 1979; Tolman, 1990). Particularly in macro-tidal regions such as the study area, tides have a significant impact on wave dynamics. Tide-induced changes in water depth and currents can alter wave heights and wave energy distributions. These changes can be more pronounced in nearshore regions, where the impact of tides is greater than that in offshore regions and characterized by shallow water (Bolaños et al., 2014). In nearshore regions, more wave energy can be funneled to the nearshore region depending on the tidal phase, and waves can reach a breaking point when the wave height exceeds a threshold relative to the local water depth (Kang and Kim, 2015). In addition, changes in current patterns can cause waves to break (Ardhuin et al., 2012). When a wave breaks, the wave energy is redistributed into the surrounding water, causing changes in the water level and current and affecting the suspension of sediments on nearshore and coastal structures. Thus, considering the alterations in wave breaking and energy distribution induced by tidal impacts in nearshore regions is crucial for coastal management and engineering practices.

5.4. Regional characteristics and improvement required for GGB

The study area is located in the eastern part of the Yellow Sea, where wind characteristics are dominated by the East Asian monsoon (Hwang et al., 2014). In the Yellow Sea, strong winter winds generate SWH of 0.9–1.9 m (Wang et al., 2019), which considerably disturbs fair-weather deposits accumulated by tidal currents, particularly in tidal flats and beaches facing the Yellow Sea (Lee, 2014). Therefore, understanding wave dynamics in nearshore regions is essential for enhancing our knowledge of sediment transport in GGB. However, wave dynamics in nearshore regions can be influenced by various factors.

First, wave-breaking regimes in nearshore regions change within a tidal cycle (Li et al., 2022a). This study demonstrated the important role of tides in the development and dissipation of waves. Moreover, owing to the shallow water depth in the intertidal zone and the macro-tidal environment of the study area, the influence in the tidal flat was more pronounced. Waves feel the bottom as the water depth changes with the tidal cycle, leading to breaking or dissipation by bottom friction. The dissipation rate of wave energy at the bottom boundary is a crucial indicator for understanding coastal environments (Kang and Di Iorio, 2006). The impact of wave energy dissipation on current disturbance and sediment resuspension owing to increasing bottom stress is an essential factor (Bolaños et al., 2014). However, this study did not consider the impact of waves on hydrodynamic conditions, which could be improved through two-way interaction with a hydrodynamic model.

Second, sediment distribution in nearshore regions plays a significant role in the propagation and dissipation of waves. For instance, waves may not break on mud flats and may be dissipated considerably by bottom friction (Le Hir et al., 2000). Therefore, understanding sediment distribution is crucial for a better understanding of wave dynamics in coastal regions (Lavaud et al., 2022). The study area is subject to a monsoonal climate, with approximately 70% of precipitation concentrated in the summer. Consequently, large amounts of suspended sediment are transported by rivers during this period. The tidal flats in GGB exhibit seasonal changes in surface texture due to wave-induced erosion in the winter and deposition from river-borne suspended sediments in the summer (Lee, 2014). However, this study did not consider the wave dynamics affected by sediment distribution, which should be included in future research. Additionally, GGB experiences continuous marine environmental changes due to landfilling, dredging, and various man-made structures, necessitating ongoing monitoring and diverse modeling approaches for accurate coastal wave dynamics modeling.

Finally, tidal flats are characterized by periodic water level fluctuations, which can impact onshore and offshore winds by heating the ground during tidal cycles (An et al., 2022). Although this study did not identify wind as the primary factor affecting periodic wave modulation, it remains a crucial determinant of wave generation and magnitude in GGB (Kang and Kim, 2015). Wind patterns, which vary depending on the tidal phase in the tidal flat, can influence wave development. Consideration of these wind effects could lead to more precise modeling of local wave development. Additionally, investigating wave development is an important area for future research as it can enhance vertical mixing in the ocean, increase sea surface roughness, and consequently impact momentum flux from the atmosphere to the ocean (Cavaleri et al., 2012).

6. Summary and conclusions

This study was aimed at investigating the factors contributing to wave modulation in GGB based on observation data and numerical model results and particularly at estimating site-specific dominant factors. The analysis of observations demonstrated that tides have a significant impact on wave dynamics at semidiurnal tidal frequencies. The nearshore region (JB) exhibited a high signal correlation of 0.62 with water elevation, while the outer region (DJ) showed a lower correlation of 0.32. Moreover, the observed SWH demonstrated spatiotemporal variability, with wave modulation being more pronounced during periods of high waves.

The numerical model successfully replicated the fundamental physical processes governing wave propagation and development and also the tidal impacts on waves. According to the model results, the dominant factor for wave modulation in the nearshore region was depth changes caused by tides. The most notable impact was observed in tidal flats, which were strongly influenced by changes in water depth. This indicates that in GGB, which features shallow water and macro-tidal, variations in water depth caused by tides are the primary cause of wave propagation and dissipation. However, currents have the potential to modulate waves depending on their relative direction to the waves; however, owing to the complex environment of GGB, spatially diverse patterns appeared even during the same tidal phase.

Cross-correlation analysis of SWH revealed that the dominant factors for wave modulation, depth, and current contribute differently across GGB. The depth dependence of wave height was mainly evident in surf zones, where the local water depth regulates wave height, with a clear distinction at locations where the ratio of wave height to water depth reached 0.2. In addition, the effect of the currents was mostly dominant in narrow channels.

To quantitatively investigate the influence of tides on waves in GGB, four additional experiments were conducted. The wave modulation in the nearshore region was revealed to be twice as dependent on tidal strength as that in the outer region. Wind was identified as the primary cause of the incoming wave height, rather than the main driver of periodic modulation. Moreover, the strength of wave modulations was found to be contingent upon the magnitude of incoming waves and tidal strength. This finding implies that wave modulation could become more intense during periods of strong tidal strength, such as spring tide, particularly when accompanied by strong winds.

CRediT authorship contribution statement

Ki-Hwan Kim: Conceptualization, Methodology, Formal analysis, Writing – original draft, Writing – review & editing. **Myung-Seok Kim:** Conceptualization, Methodology, Formal analysis, Writing – original draft, Writing – review & editing. **Hye Min Lee:** Data curation,

Validation. **Myung Hwan Kim:** Data curation, Validation. **Seung-Buhm Woo:** Conceptualization, Writing – review & editing, Project administration, Funding acquisition.

Declaration of competing interest

The authors declare that they have no known competing financial interests or personal relationships that could have appeared to influence the work reported in this paper.

Data availability

Data will be made available on request.

Acknowledgments

This work was supported by Institute of Information & communications Technology Planning & Evaluation (IITP) grant funded by the Korea government (MSIT) (RS-2022-00155915, Artificial Intelligence Convergence Innovation Human Resources Development (Inha University)). This research was supported by Korea Institute of Marine Science & Technology Promotion (KIMST) funded by the Ministry of Oceans and Fisheries, Korea (20220051 Gyeonggi-Incheon SeaGrant).

References

Aboobacker, V., Vethamony, P., Samiksha, S., Rashmi, R., Jyoti, K., 2013. Wave transformation and attenuation along the west coast of India: measurements and numerical simulations. Coast Eng. J. 55 (1), 1350001 https://doi.org/10.1142/S0578563413500010.

Allahdadi, M.N., He, R., Neary, V.S., 2019. Predicting ocean waves along the US east coast during energetic winter storms: sensitivity to whitecapping parameterizations. Ocean Sci. 15, 691–715. https://doi.org/10.5194/os-15-691-2019.

An, H.Y., Jeong, J.H., Kang, Y.H., Lee, H.J., Kim, Y.K., 2022. Assessing the meteorological impacts of time-varying land cover in the intertidal zone. J. Geophys. Res. Atmos. 127 (7), e2021JD034927 https://doi.org/10.1029/2021JD034927.

Ardhuin, F., Roland, A., Dumas, F., Bennis, A., Sentchev, A., Forget, P., Wolf, J., Girard, F., Osuna, P., Benoit, M., 2012. Numerical wave modeling in conditions with strong currents: dissipation, refraction, and relative wind. J. Phys. Oceanogr. 42 (12), 2101–2120. https://doi.org/10.1175/JPO-D-11-0220.1.

Bolaños, R., Brown, J.M., Souza, A.J., 2014. Wave–current interactions in a tide dominated estuary. Continent. Shelf Res. 87, 109–123. https://doi.org/10.1016/j.csr.2014.05.009.

Booij, N., Ris, R.C., Holthuijsen, L.H., 1999. A third-generation wave model for coastal regions: 1. model description and validation. J. Geophys. Res.: Oceans 104, 7649–7666. https://doi.org/10.1029/98JC02622.

Byun, D.S., Choi, B.J., Hart, D.E., 2023. Overcoming tide-related challenges to successful regional and coastal ocean modeling. Front. Mar. Sci. 10, 541. https://doi.org/10.3389/fmars.2023.1150305.

Cavaleri, L., Barbariol, F., Benetazzo, A., 2020. Wind–wave modeling: where we are, where to go. J. Mar. Sci. Eng. 8 (260), 1–15. https://doi.org/10.3390/jmse8040260.

Cavaleri, L., Fox-Kemper, B., Hemer, M., 2012. Wind waves in the coupled climate system. Bull. Am. Meteorol. Soc. 93 (11), 1651–1661. https://doi.org/10.1175/BAMS-D-11-00170.1.

Chen, C., Liu, H., Beardsley, R.C., 2003. An unstructured grid, finite-volume, three-dimensional, primitive equations ocean model: application to coastal ocean and estuaries. J. Atmos. Ocean. Technol. 20, 159–186. https://doi.org/10.1175/1520-0426(2003)020<0159:AUGFVT>2.0.CO;2.

Choi, J.K., Park, Y.J., Lee, B.R., Eom, J., Moon, J.E., Ryu, J.H., 2014. Application of the Geostationary Ocean Color Imager (GOCI) to mapping the temporal dynamics of coastal water turbidity. Remote Sens. Environ. 146, 24–35. https://doi.org/10.1016/j.rse.2013.05.032.

Dodet, G., Melet, A., Ardhuin, F., Bertin, X., Idier, D., Almar, R., 2019. The contribution of wind-generated waves to coastal sea-level changes. Surv. Geophys. 40 (6), 1563–1601. https://doi.org/10.1007/s10712-019-09557-5.

Egbert, G.D., Erofeeva, S.Y., 2002. Efficient inverse modeling of barotropic ocean tides. J. Atmos. Ocean. Technol. 19 (2), 183–204. https://doi.org/10.1175/1520-0426(2002)019<0183:EIMOBO>2.0.CO;2.

Holthuijsen, L.H., 2010. Waves in Oceanic and Coastal Waters. Cambridge University Press, Cambridge. https://doi.org/10.1017/CBO9780511618536.

Hwang, J.H., Van, S.P., Choi, B.J., Chang, Y.S., Kim, Y.H., 2014. The physical processes in the Yellow Sea. Ocean Coast Manag. 102, 449–457. https://doi.org/10.1016/j.ocecoaman.2014.03.026.

Kang, K., Di Iorio, D., 2006. Depth- and current-induced effects on wave propagation into the Altamaha River Estuary, Georgia. Estuar. Coast Shelf Sci. 66 (3–4), 395–408. https://doi.org/10.1016/j.ecss.2005.09.008.

Kang, K., Kim, S., 2015. Wave–tide interactions during a strong storm event in Kyunggi Bay, Korea. Ocean. Eng. 108, 10–20. https://doi.org/10.1016/j.oceaneng.2015.07.024.

Kim, B.O., 2003. Tidal modulation of storm waves on a macrotidal flat in the Yellow Sea. Estuar. Coast Shelf Sci. 57 (3), 411–420. https://doi.org/10.1016/S0272-7714(02)00369-4.

Kim, M.S., Woo, S.B., Eom, H., You, S.H., Lee, H.M., 2022. Towards observation-and atmospheric model-based early warning systems for meteotsunami mitigation: a case study of Korea. Weather Clim. Extrem., 100463 https://doi.org/10.1016/j.wace.2022.100463.

Kim, S.Y., Yasuda, T., Mase, H., 2008. Numerical analysis of effects of tidal variations on storm surges and waves. Appl. Ocean Res. 30 (4), 311–322. https://doi.org/10.1016/j.apor.2009.02.003.

Komen, G.J., Hasselmann, S., Hasselmann, K., 1984. On the existence of a fully developed wind-sea spectrum. J. Phys. Oceanogr. 14 (8), 1271–1285. https://doi.org/10.1175/1520-0485(1984)014<1271:OTEOAF>2.0.CO;2.

Lai, R.J., Long, S.R., Huang, N.E., 1989. Laboratory studies of wave-current interaction: kinematics of the strong interaction. J. Geophys. Res.: Oceans 94 (C11), 16201–16214. https://doi.org/10.1029/JC094iC11p16201.

Lavaud, L., Bertin, X., Martins, K., Pezerat, M., Coulombier, T., Dausse, D., 2022. Wave dissipation and mean circulation on a shore platform under storm wave conditions. J. Geophys. Res.: Earth Surf. 127 (3), e2021JF006466 https://doi.org/10.1029/2021JF006466.

Le Hir, P., Roberts, W., Cazaillet, O., Christie, M., Bassoullet, P., Bacher, C., 2000. Characterization of intertidal flat hydrodynamics. Continent. Shelf Res. 20 (12–13), 1433–1459. https://doi.org/10.1016/S0278-4343(00)00031-5.

Lee, H.J., 2014. A review of sediment dynamical processes in the west coast of Korea, eastern Yellow Sea. Ocean Sci. J. 49 (2), 85–95. https://doi.org/10.1007/s12601-014-0010-0.

Li, Y., Zhang, C., Song, J., Chi, S., Zhao, S., Qi, H., Shi, J., 2022a. Tide-modulated wave characteristics and breaking regimes in the intertidal zone of a dissipative beach. Ocean Eng. 266, 113055 https://doi.org/10.1016/j.oceaneng.2022.113055.

Li, Z., Li, S., Hou, Y., Mo, D., Li, J., Yin, B., 2022b. Typhoon-induced wind waves in the northern East China Sea during two typhoon events: the impact of wind field and wave-current interaction. J. Oceanol. Limnology 1–16. https://doi.org/10.1007/s00343-021-1089-7.

Mei, C.C., 1983. The Applied Dynamics of Ocean Surface Waves. Wiley, New York. https://doi.org/10.1142/0752.

Moon, I.J., 2005. Impact of a coupled ocean wave-tide-circulation system on coastal modeling. Ocean Model. 8 (3), 203–236. https://doi.org/10.1016/j.ocemod.2004.02.001.

Power, H.E., Hughes, M.G., Aagaard, T., Baldock, T.E., 2010. Nearshore wave height variation in unsaturated surf. J. Geophys. Res.: Oceans 115 (C8). https://doi.org/10.1029/2009JC005758.

Seo, S.N., 2008. Digital 30sec gridded bathymetric data of Korea marginal seas-KorBathy30s. J. Korean Soc. Coast. Ocean Eng. 20 (1), 110–120 (in Korean). https://www.dbpia.co.kr/pdf/pdfView.do?nodeId=NODE06219970.

Sirisha, P., Remya, P.G., Srinivas, K., Nair, T.B., 2023. Wave modulations in the Indian coastal area due to wave–tide interactions. J. Earth Syst. Sci. 132 (1), 17. https://doi.org/10.1007/s12040-022-02035-4.

Song, H., Kuang, C., Wang, X.H., Ma, Z., 2020. Wave-current interactions during extreme weather conditions in southwest of Bohai Bay, China. Ocean Eng. 216, 108068 https://doi.org/10.1016/j.oceaneng.2020.108068.

Sun, W., Liang, B., Shao, Z., Wang, Z., 2022. Analysis of Komen scheme in the SWAN model for the whitecapping dissipation during the tropical cyclone. Ocean Eng. 266, 113060 https://doi.org/10.1016/j.oceaneng.2022.113060.

Thornton, E.B., Guza, R.T., 1982. Energy saturation and phase speeds measured on a natural beach. J. Geophys. Res.: Oceans 87 (C12), 9499–9508. https://doi.org/10.1029/JC087iC12p09499.

Tolman, H.L., 1990. The influence of unsteady depths and currents of tides on wind-wave propagation in shelf seas. J. Phys. Oceanogr. 20 (8), 1166–1174. https://doi.org/10.1175/1520-0485(1990)020<1166:TIOUDA>2.0.CO;2.

Torrence, C., Compo, G.P., 1998. A practical guide to wavelet analysis. Bull. Am. Meteorol. Soc. 79 (1), 61–78. https://doi.org/10.1175/1520-0477(1998)079<0061:APGTWA>2.0.CO;2.

Viitak, M., Maljutenko, I., Alari, V., Suursaar, Ü., Rikka, S., Lagemaa, P., 2016. The impact of surface currents and sea level on the wave field evolution during St. Jude storm in the eastern Baltic Sea. Oceanologia 58 (3), 176–186. https://doi.org/10.1016/j.oceano.2016.01.004.

Vincent, C.E., 1979. The interaction of wind-generated sea waves with tidal currents. J. Phys. Oceanogr. 9 (4), 748–755. https://doi.org/10.1175/1520-0485(1979)009<0748:TIOWGS>2.0.CO;2.

Wang, A., Ralston, D.K., Bi, N., Cheng, Z., Wu, X., Wang, H., 2019. Seasonal variation in sediment transport and deposition on a muddy clinoform in the Yellow Sea. Continent. Shelf Res. 179, 37–51. https://doi.org/10.1016/j.csr.2019.04.009.

Wang, P., Sheng, J., 2018. Tidal modulation of surface gravity waves in the Gulf of Maine. J. Phys. Oceanogr. 48 (10), 2305–2323. https://doi.org/10.1175/JPO-D-17-0250.1.

Whitham, G.B., 1974. Linear and Nonlinear Waves. Wiley, New York. https://doi.org/10.1002/9781118032954.

Wolf, J., Brown, J.M., Bolanos-Sanchez, R., Hedges, T.S., 2011. Waves in coastal and estuarine waters. Treatise Estuar. and Coast. Sci. 2, 171–212. https://doi.org/10.1016/B978-0-12-374711-2.00203-5.

Wolf, J., Prandle, D., 1999. Some observations of wave-current interaction. Coast. Eng. 37 (3), 471–485. https://doi.org/10.1016/S0378-3839(99)00039-3.

Woo, S.B., Yoon, B.I., 2011. The classification of estuary and tidal propagation characteristics in the Gyeong-Gi Bay, South Korea. J. Coast Res. 1624–1628. https://www.jstor.org/stable/26482450.

Yoo, S.C., Mun, J.Y., Park, W., Seo, G.H., Gwon, S.J., Heo, R., 2019. Development of bathymetric data for ocean numerical model using sea-floor topography data: BADA Ver.1. J. Korean Soc. of Coast. Ocean Eng. 31 (3), 146–157. https://doi.org/10.9765/KSCOE.2019.31.3.146 (in Korean).

Yu, X., Pan, W., Zheng, X., Zhou, S., Tao, X., 2017. Effects of wave-current interaction on storm surge in the Taiwan Strait: insights from Typhoon Morakot. Continent. Shelf Res. 146, 47–57. https://doi.org/10.1016/j.csr.2017.08.009.

Zijlema, M., 2010. Computation of wind-wave spectra in coastal waters with SWAN on unstructured grids. Coast. Eng. 57 (3), 267–277. https://doi.org/10.1016/j.coastaleng.2009.10.011.